

# Landslide rupture and length-depth scaling

Colin P. Stark

Lamont-Doherty Earth Observatory, Columbia University, Palisades, New York, USA.

Eunseo Choi

Center for Earthquake Research and Information, University of Memphis, Memphis, Tennessee, USA.

## Abstract.

Landslides are often assumed to exhibit self-similarity in their failure geometry and a linear scaling between slip depth and rupture length. Such an assumption has important implications for the prediction of large landslide volumes and for the estimation of erosion budgets by mass-wasting. However, some field data indicate a break from self-similarity and imply that in some circumstances landslide depth may scale non-linearly with length. Here we test the simple scaling hypothesis by numerical experiment. Modeling is performed with SNAC (StGermaiN Analysis of Continua), a 3D community code originally designed to model elastoviscoplastic deformation on a crustal scale and newly adapted to treating hillslope failure. SNAC employs a parallelized, Lagrangian, explicit finite-difference scheme and dynamic relaxation to solve static, quasi-static and steady-state problems. Landslide rupture is treated as emergent shear localization under strain-weakening Mohr-Coulomb plasticity. We model only the initial slip and early motion of a landslide; granular flow during the runout phase is not considered. A set of 2+1D simulations of failures spanning lengths of 50–400 m suffice to vindicate cross-sectional self-similarity—absent any dominant depth scale or trend in the variation of cohesion—and a depth-length ratio of 11–15% is recorded. An interesting by-product of the choice of experimental geometry is some unanticipated complexity in the evolution of the slip plane. Failure initiates at the toe, propagates upslope, and asymptotically parallels the planar upper boundary. However, a connected failure surface is only achieved once a secondary rupture has propagated downwards into this slip plane from the upper breakaway zone. The broader outcome of our numerical experiments is a demonstration of how 3D continuum modeling of soil and rock-slope failure, and the study of their rich behavior, is now feasible using non-commercial code on supercomputing platforms.

## 1. Introduction

Opinions differ as to the systematic relationship between landslide rupture depth  $z$  and rupture length  $L$  [Guzzetti *et al.*, 2009], and there is correlative disagreement over the corresponding scaling of rupture area  $A$  with mobilized debris volume  $V$  [Brunetti *et al.*, 2009; Malamud *et al.*, 2004b]. The diversity of opinion originates in the broad spectrum of scaling constraints provided by landslide field studies.

Some empirical studies infer a square root relationship  $z \sim \sqrt{A}$  between slip depth  $z$  and slip area  $A$ , which is equivalent to deducing both simple geometric scaling  $V \sim A^{3/2}$  of mobilized debris volume  $V$  with slip area and a linear dependence  $z \sim L$  of rupture depth on rupture length  $L$  [Guzzetti *et al.*, 2008; Hovius *et al.*, 1997; Malamud *et al.*, 2004a, b; Stark and Guzzetti, 2009]. Others indicate that rupture depth is approximately constant or scales weakly with length  $L$ , which suggests a roughly linear scaling between slip area  $A$  and volume  $V$  [Abele, 1974; Guthrie and Evans, 2004; Larsen and Montgomery, 2008; Martin *et al.*, 2002; Rice and Foggia, 1971]. Yet others infer anomalous (not simply geometrical) scaling between depth and area  $z \sim A^{\eta/2} \sim L^{\eta}$  with fractional exponents largely spanning  $0 \leq \eta \leq 1$  [Imaizumi and Sidle, 2007; Imaizumi *et al.*, 2008; Innes, 1983; Korup, 2005; Simonett, 1967; Whitehouse, 1983] (there is some overlap between the last two categories).

There are two reasons for this empirical ambiguity: (1) natural complexity; (2) observational error.

First, the variety and complexity of mass-wasting processes complicate scaling analyses of field data. The modes and mechanisms of slope failure vary from one landslide inventory to another, as do the climatic and hydrologic environments, the ecological settings, the landscape relief, the thicknesses of failing soil and regolith, the geology of failing bedrock, and the geometry of failure relative to bedrock anisotropy, i.e., cleavage or bedding plane-parallel slip or otherwise.

For example, on some failing slopes with well-developed soils and a marked variation in cohesive strength with depth, landslide thickness appears largely independent of length [Larsen and Montgomery, 2008]. In contrast, the collapse of bedrock slopes where regolith is poorly developed [Hovius *et al.*, 1997], or where regolith and bedrock exhibit similarly low cohesive strength [Cardinali *et al.*, 2001; Guzzetti *et al.*, 2009], appears to yield landslides whose thickness is proportional to failure length.

Second, the field measurement of 3D landslide geometry is a challenging process prone to large errors that limit the robustness of scaling analyses. The majority of field studies record rough estimates of slide thickness for only a few, big failures ( $O\{N\} = 10\text{--}100$ ,  $L > 50$  m), i.e., not across a broad range of scales. They typically deduce the source (rupture) area  $A$  from the directly observed, total disturbed area  $A_t$  by assuming a linear scaling between the two  $A_t \sim A$ , and this assumption may distort estimation of the correct scaling relation between rupture area and thickness. In rare cases an attempt is made to measure the landslide source

area explicitly but such an endeavor leads to errors of its own [Hovius *et al.*, 1997; Stark and Hovius, 2001].

Given these complexities, it is not surprising that general conclusions regarding the geometric scaling of slope failure are difficult to make. Nevertheless, disambiguation of the controls on such scaling is needed if we are to understand better the role of mass wasting in the erosion of mountain landscapes [Brardinoni and Church, 2004; Dadson *et al.*, 2003; Dietrich and Dunne, 1978; Dietrich *et al.*, 2003; Hovius and Stark, 2006; Korup, 2006; Martin *et al.*, 2002; Ohmori and Hirano, 1988; Sidle and Ochiai, 2006; Sugai and Ohmori, 1994]. Progress is particularly needed in understanding landslide volume-area scaling, since it plays an important role in linking empirical estimates of landslide area distribution  $p(A)$  to the mass-wasting sediment budget [Guzzetti *et al.*, 2009; Hovius *et al.*, 1997; Kelsey, 1980; Lavé and Burbank, 2004; Malamud *et al.*, 2004a; Stark and Guzzetti, 2009].

## 2. Hypothesis

We pose the hypothesis that, in the absence of material and topographic complexity, the maximum depth of landslide rupture scales linearly with rupture length. Initial landslide failure geometry is strictly self-similar in such a hypothesis and the scaling relations are simple. There is a linear scaling between maximum rupture depth  $z_m$  (measured vertically) and planform rupture length  $L$  (measured horizontally),

$$z_m = \eta L \quad (1)$$

where  $\eta$  is a dimensionless depth-length ratio, and simple geometric scaling of mobilized debris volume  $V$  and rupture area  $A$ ,

$$V \sim A^{3/2} \quad (2)$$

since we also assume that planform rupture area  $A$  scales geometrically with rupture length

$$A \sim L^2. \quad (3)$$

The latter equation requires that the planform shape of landslide failure (source slip area) be the same regardless of the scale of failure, which seems generally to be the case for most types of landslide failure, although quantitative assessments are rare [Hovius *et al.*, 1997].

The self-similar length-depth scaling hypothesis was first made in the context of landslide area-volume distributions and sediment budget estimation by Hovius *et al.* [1997] and has been used on several occasions since [e.g., Guzzetti *et al.*, 2009; Lavé and Burbank, 2004; Malamud *et al.*, 2004b]. It is often implicit in engineering assessments of slope failure, particularly in modeling treatments that impose an anticipated slip plane in the assessment of a safety factor [e.g., Morgenstern and Price, 1965; Wyllie and Mah, 2004]. Linear scaling is also broadly consistent with geotechnical modeling where the plane of failure is not predetermined, for example in studies using commercial codes such as FLAC, FLAC-3D, ELFEN, PFC, Tochnog and UDEC [Barla, 2008; Brideau *et al.*, 2006; Commend *et al.*, 2004; Crosta *et al.*, 2003; Crosta and Clague, 2006; Evans *et al.*, 2006; Li *et al.*, 2006; Pasculli and Sciarra, 2006; Poisel *et al.*, 2009; Stead *et al.*, 2006]. However, no systematic assessment of geometrical scaling using these or other codes has yet been attempted.

## 3. Experiments

We tested the linear scaling hypothesis by conducting a set of numerical experiments in which the length scale of plastic failure was strictly controlled. The experimental

geometry is shown in Figure 1. A two-dimensional cross-section was deemed sufficient to carry out the test, even though the modeling framework (SNAC) is entirely capable of handling 3D deformation [Choi *et al.*, 2008]. In fact, the model grid was one cell wide in the  $z$ -horizontal direction, and the full three-dimensional stress and strain tensors were computed, thus making the simulations effectively 2+1D.

### Rheological model

Discontinuous structures such as faults and cracks are often modeled as strain localization, in a continuum sense, in inelastic (aka anelastic) media [e.g., Choi *et al.*, 2008; Cundall, 1989; Gerbault *et al.*, 1998; Lavier *et al.*, 2000; Poliakov *et al.*, 1994; Rice, 1976; Rudnicki, 1984; Templeton and Rice, 2008]. One justification for this approach is that “effective” material properties are sufficient to describe the geometry of discontinuities and the global behavior of material including them. Strain weakening (or softening) plasticity is a constitutive model for materials having negative stiffness after yielding and it has been shown to unconditionally cause localization [Rudnicki and Rice, 1975]. SNAC combines Mohr-Coulomb plasticity with piecewise-linear strain weakening [Choi *et al.*, 2008; Lavier *et al.*, 2000], in which cohesion decreases monotonically with plastic strain. **TKTK: Expand here, because rheology is super important.**

### Numerical method: SNAC

**TKTK: Maybe there are more recent refs here now?**

SNAC (StGermaiN Analysis of Continua) is a parallel, Lagrangian, explicit finite difference code for solving solid mechanical problems. SNAC is built upon a scientific software framework called StGermain [Quenette *et al.*, 2005], which provides the generic libraries and data structures frequently needed for numerical modeling. For instance, input file handling and parallelization through domain decomposition are already implemented within StGermain so that higher level applications like SNAC can simply re-use such functionality. SNAC and StGermain are distributed under a GNU Public License by the Cyber Infrastructure for Geodynamics (CIG).

SNAC uses the momentum balance equation in its dynamic form, but seeks quasi-static solutions via dynamic relaxation [Cundall, 1987; Day, 1965; Hodgkins, 1967; Otter, 1965; Otter *et al.*, 1966; Underwood, 1983]. Dynamic relaxation is achieved by adding a damping force at each node whose magnitude is proportional to that of the unbalanced force at the node. This type of damping has several advantages over conventional velocity-based (viscous) damping [Otter *et al.*, 1966], from a computational efficiency perspective, in that static or steady-state solutions are achieved more rapidly and more accurately [Cundall, 1987].

SNAC employs an energy-based discretization technique [Bathe, 1996] that can broadly be classified as a finite difference method, but which is also equivalent to the finite element (FE) method in the sense that the weak forms of the governing equations are discretized. Consequently, SNAC shares some of the benefits of an explicit FE code. However, one major difference with an FE code is that partial derivatives are defined through an integral identity [Wilkins, 1964] rather than in terms of derivatives of shape functions.

The explicit scheme makes it relatively easy to implement complicated constitutive models, because there is no need for the multiple stress updates at each time step required in an implicit method. Although the conditional stability of explicit time integration sometimes leads to a prohibitively small time-step size, we increase it to a reasonably large value through mass scaling [Cundall, 1987].

More details on the implementation of SNAC are given in the Appendix.

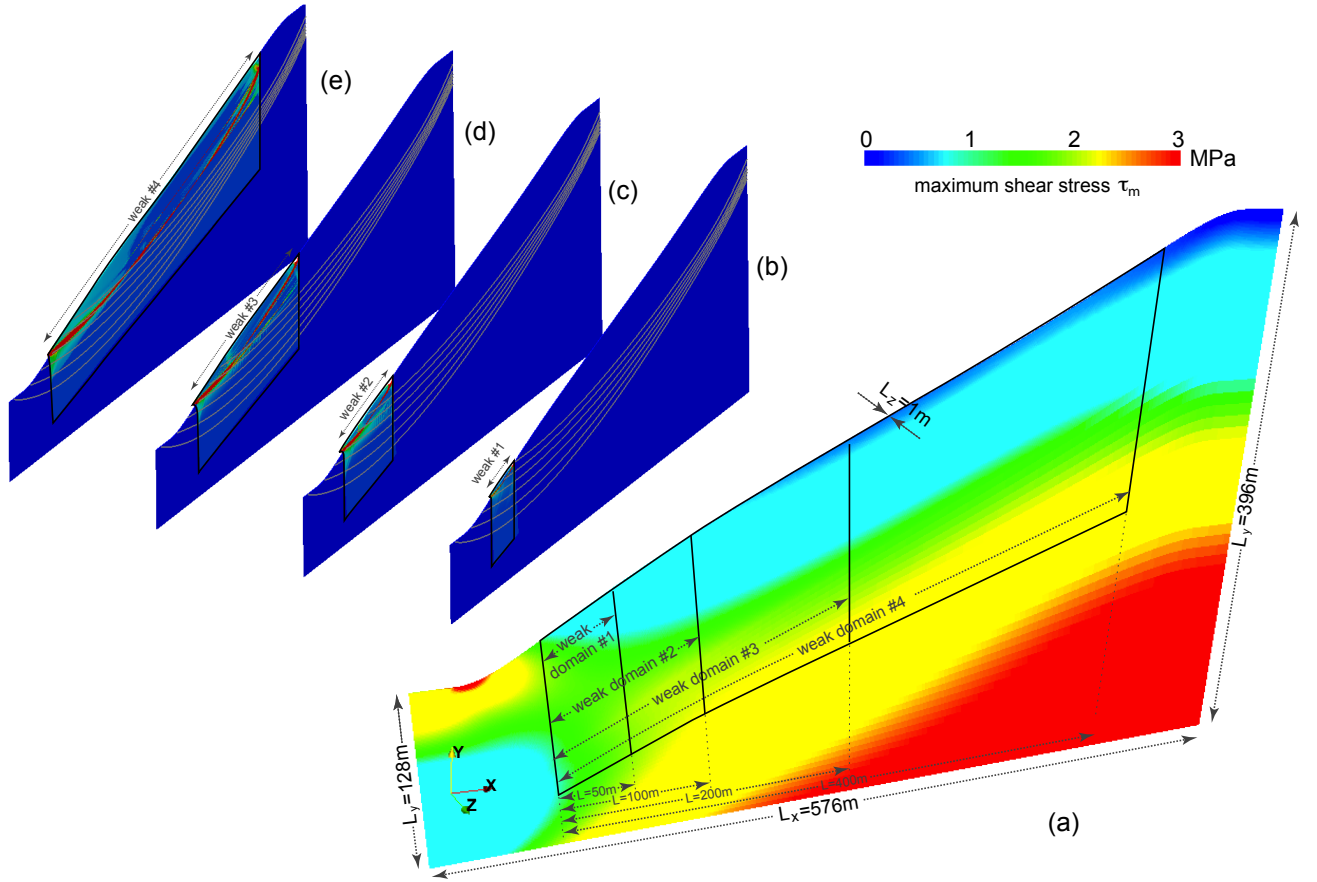


**Figure 1: TKTK: Update needed here.** Model geometry and initial elastic stress state (perspective view). The 3D step-ramp-step mesh used in the numerical simulations is shown after elastic equilibration (Stage 1) has been achieved. The color contours indicate the state of maximum shear stress  $\tau_m$  prior to the imposition of a sub-domain of low cohesion (Stage 2) in order to trigger localized plastic failure and landslide motion. Each sub-domain is indicated by black solid or dashed lines for  $L = 50$  m (experiments  $N = 1, 2$ ),  $L = 100$  m ( $N = 3, 4$ ),  $L = 200$  m ( $N = 5$ ), and  $L = 400$  m ( $N = 6 - 8$ ; see Table 1).

### Geometry, parameters, and boundary conditions

The model geometry took the sigmoidal form of a step-ramp-step with a long, planar (prior to elastic deformation) ramp dipping at a uniform angle of  $\theta = 30^\circ$ . Landslide simulations were confined to the planar domain in order to minimize topographic effects on the pattern of elastic stresses driving failure. As Figure 1 shows, the central planar domain has a maximum extent of 400 m with shear stress contours lying sub-parallel to and tapering down into its upper boundary [Martel and Muller, 2000; Muller and Martel, 2000; Martel, 2000].

The material parameters were chosen as follows: density  $\rho = 2500 \text{ kg/m}^3$ , which is consistent with soil and low-density rock; Lamé elastic constants  $\lambda = 10 \text{ MPa}$  and  $\mu = 10 \text{ MPa}$ , which are consistent with soil and low rigidity rock, and which together define a Poisson's ratio of  $\nu = 0.25$  and a Young's modulus of  $E = 25 \text{ MPa}$ ; background cohesion  $c_b = 3 \text{ MPa}$  (imposed throughout the grid during the elastic equilibration stage); Coulomb angle of friction  $\phi = 25^\circ$ ; dilatancy angle  $\psi = 5^\circ$ .

The domain was a 3D mesh with the following dimensions:  $L_x = 576$  m left to right;  $L_z = 1$  m front to back; vertically  $L_y = 128$  m at the left boundary  $x = 0$ , and  $L_y = 396$  m at the right boundary  $x = L_x$ . The boundary conditions were defined in terms of the veloc-

ity components  $v_j$  of boundary mesh nodes: (a) on the narrow left and right surfaces, where  $x = 0$  and  $x = L_x$  respectively,  $x$ -horizontal motion was suppressed with  $v_x = 0$ , but other motions were allowed (free slip in  $y$  and  $z$ ) with  $v_y$  and  $v_z$  undefined; (b) on the bottom surface, where  $y = 0$ , motion was suppressed in all directions with  $v_x = v_y = v_z = 0$ ; (c) motion was unconstrained on the top surface; (d) on the front and back surfaces, where  $z = 0$  and  $z = L_z$  respectively,  $z$ -horizontal motion was suppressed with  $v_z = 0$ , but other motions were allowed (free slip in  $x$  and  $y$ ) with  $v_x$  and  $v_y$  undefined. The effect of these boundary velocity constraints was to pin the base ( $z = 0$ ) to a horizontal plane, and to make the vertical sides act as reflecting boundary conditions. The upper boundary was completely free to move and acted as if its surface pressure were zero (atmospheric pressure is ignored).

Solution was performed on a structured (topologically regular) mesh composed of  $576 \times 128 \times 1$  hexahedral cells, each containing two overlapping sets of five tetrahedra—numerical stress calculations are performed separately on each set of tetrahedra and then merged to achieve a more stable solution for that time step (see Appendix). Computation was conducted in parallel by dividing the domain into an array of  $16 \times 4 \times 1 = 64$  blocks, each of which was assigned to a different processor core.

To ensure greater fidelity of numerical solution, distortion of the initial size and shape of the hexahedral cells was kept to a minimum in the upper part (extending from the upper boundary down to about  $\approx 100$  m) of the mesh: in this zone, the size of the cells was a uniform  $1 \text{ m}^3$  and their shape was maintained as close to cubic as possible; below this zone the cells were stretched towards the horizontal base such that the mesh geometry in Figure 1 was achieved. All the cells ultimately involved in strain localization and shear zone formation, which were located in the upper part of the central planar-dipping region, had an initial geometry of a parallelepiped (Figure 4).

The step-ramp-step is a standard model geometry in geotechnical engineering treatments of slope stability (e.g., in FLAC Slope), but such treatments differ from our experiments in that they typically allow plastic failure to take place throughout the model domain. As a result, landslide rupture invariably begins at the shear stress concentration at the bottom step (shown in red in Figure 1) and propagates in a curved fashion towards a breakaway zone within the top step. We chose to limit all model failures to sub-domains within the ramp so as to avoid the stress-focusing effects of the steps. Nevertheless, the full step-ramp-step geometry was used instead of a pure ramp in order to maximize topographic smoothness across the left and right (reflecting) bound-

aries and to minimize any attendant stress distortions near these edges.

### Stage 1: Elastic equilibrium

The first stage of the experiment, prior to any simulation of plastic failure and landslide rupture, was to treat the model cross-section as a purely elastic body deforming under its own weight and to solve for static elastic equilibrium. This was achieved in SNAC by allowing the initially unstressed mesh geometry to subside under its body forces, and to solve for the transmission of stress by modeling the propagation and attenuation of elastic waves throughout the mesh. Simulation duration was maintained for a large number of time steps ( $\mathcal{O}\{t\} \approx 5 \times 10^5$ ) to guarantee sufficient relaxation to occur and for elastic equilibrium to be reached. Figure 1a visualizes one aspect of the Cauchy stress tensor, the maximum shear stress  $\tau_m$ , at static equilibrium.

### Stage 2: Elastoplastic deformation

In the second stage of the experiment, we generated a set of model landslides across a range of length scales, starting in each case with the domain in static elastic equilibrium. The scale of each failure was controlled by: (a) selecting a sub-domain of mesh nodes located flush with the left-hand edge of the central (initially planar) hillslope (Figure 1); (b) choosing the upslope width of this sub-domain to be  $L = 50 \text{ m}$ ,  $L = 100 \text{ m}$ ,  $L = 200 \text{ m}$ , or  $L = 400 \text{ m}$  (Table 1, Figures 1; 4); (c) fixing the sub-domain depth at 100 m from the upper boundary (Figure 1) at the left edge (the depth increases slightly to the right); (d) reducing cohesion within this sub-domain from the high background value of  $c_b = 3 \text{ MPa}$  to values ranging from  $c = 10 \text{ kPa}$  to  $c = 30 \text{ kPa}$  (Table 1).

Such a reduction of cohesion in this elastically stressed Mohr-Coulomb material immediately induces plastic yield throughout the sub-domain (Figures 4, 2–5), given that the topographic slope is around  $\theta = 30^\circ$ , the friction angle is  $\phi = 25^\circ$ , and that shear stresses reach  $1 \text{ MPa}$  within 50 m of the upper boundary.

### Implementation of strain-weakening plasticity

The strain-weakening model employed in our experiments was effectively a linear model of cohesion decrease with plastic strain. Cohesion was required to drop from the initial sub-domain value  $c$  at a strain of  $\epsilon \approx 0$  down to  $3 \text{ kPa}$  at a strain of  $\epsilon = 1$ . To ensure computational stability for greater plastic strains, a further linear drop down to a cohesion of  $30 \text{ Pa}$  at  $\epsilon = 1000$  was imposed; however, the experiments were terminated once plastic strain much above  $\epsilon = 2$  was achieved, because accurate computation of the tetrahedral stress-strain tensors is compromised once the structured mesh is severely distorted. **TKTK: Thus: no need to say this?** No commensurate changes in the angle of friction  $\phi$  or the dilatancy angle  $\psi$  were modeled, although SNAC can accommodate both.

## 4. Results

### Rupture propagation

In all the experiments in which landslides were triggered, we observed a consistent pattern of initial slip, rupture propagation, merging of slip planes, shear within the landslide body, and oscillatory background plastic deformation. The behavior is illustrated in Figures 2–5 for sub-domain scale  $L = 400$  m and in Figure 4 for each sub-domain scale.

<sup>EC</sup>: [Added the following two paragraphs.] On top of the second invariant of plastic strain, we plot slip lines, i.e., the trajectories of local failure directions, in Figures 2 and 3. Conjugate shear failure directions can be locally determined based on a given stress field and are supposed to make an acute angle from the maximum compressional principal stress. However, the orientation of shear localization under a strain softening plasticity is known to be indeterminate between the Coulomb (in the current definition,  $45^\circ - \phi/2$  where  $\phi$  is a friction angle) and the Roscoe angle ( $45^\circ - \psi/2$  where  $\psi$  is a dilation angle) [e.g. *Vermeer and de Borst*, 1984]. For this reason, the Arthur angle, the median of the two, is adopted here to represent failure direction. Once the maximum compressional principal stress is calculated (pale pink rods in Figures 2 and 3), the conjugate failure directions (dark pink rods) are easily acquired by rotating it clockwise and anti-clockwise by the Arthur angle.

The slip lines in Figure 2a, for instance, can be interpreted as possible failure geometry as in the traditional slip line analysis. However, it is notable that the slip lines in Figure 2a completely fails to predict the actual rupture plane (Figure 2f). The main reason is that the slip line solutions in Figure 2a are determined solely by the stresses in elastic equilibrium and therefore fails to capture the effects of heterogeneity in the subdomain as well as dynamic change in stresses due to rupture propagation.

At the onset of Stage 2 in each experiment, when the chosen sub-domain was subject to a drop in cohesion, each sub-domain instantly experienced a broadly homogeneous plastic deformation. Since the mesh beyond (down and to the left of) the sub-domain remained too strong to permit plastic yield, the lower left boundary acted as a semi-rigid buttress. As a result, plastic deformation rapidly began to focus at the downslope upper corner of the sub-domain (Figures 2<sup>EC</sup>:ab, 5a). In all the experiments except  $N = 2$  this zone of deformation evolved by strain weakening into a narrow rupture zone. This zone was initially horizontal and propagated into (right) and up the slope in a curvilinear fashion (Figures 2b, 5a, 5b).

Each rupture grew asymptotically into parallelism with the upper surface (and with local orientation of the mesh geometry) at a depth  $z_m$  that scaled with the

width of the deforming sub-domain  $L$  (Figures 2<sup>EC</sup>:bc, 5b). Propagation continued until the ruptures reached the upper right edge of the sub-domain (Figures 2c, 5c), at which point deformation switched to the incipient breakaway region immediately above.

Short, downslope-dipping shear zones were observed to form in this upper region near the surface and migrate vertically downwards in a wave-like fashion while extending downslope in parallel with the main down-going rupture (remnants of these migrating shear zones can be seen in at the top-right of the sub-domains in Figures 2d, 5d), eventually forming several focused slip zones through strain weakening. One of these downward-propagating ruptures succeeded in linking with the main rupture to form one contiguous slip surface (Figures 2e, 5e) and a complete landslide (Figures 2f, 5f, 5f).

The trajectories of each linking downward-growing rupture varied with each experiment, and the variable linking geometry goes a long way to explaining the observed spread of depth-length ratios and imperfect geometric self-similarity (Table 1). This behavior is most evident when comparing Figures 4b, 4c, 4d and Figure 2f. Variability in trajectory geometry probably occurs because of sensitivity in the downward-growing ruptures to weak, transient heterogeneity in the numerically computed stress and strain fields. Such heterogeneity (visible in Figure 5) originates in the (effectively stochastic) interference of elastic waves radiated from elastoplastically straining regions that are reflected and refracted at domain boundaries and density interfaces. Material heterogeneity would almost certainly have a similar but stronger randomizing effect, and future experiments will investigate the effects of stochasticity further.

### Secondary deformation

Several secondary but nevertheless interesting deformation features recurred in each experiment.

(a) A sub-vertical wedge of diffuse plastic deformation developed at the <sup>EC</sup>:upper [maybe ‘top’ is better?]-left edge of the sub-domain very early in Stage 2 (e.g., Figure 2a) <sup>EC</sup>: [b rather than a?]. Although this region is not the location of <sup>EC</sup>:global shear stress concentration, which instead lies below the lower step (Figure 1), it is the zone of greatest initial shear stress in the sub-domain <sup>EC</sup>: {at the beginning of Stage 2<sup>EC</sup>:}. Only a small portion of this zone experienced significant strain weakening and the kind of deformation focusing that generated landslide rupture (exemplified in Figure 2).

(b) As Figures 4a, 4b show, the left-hand steeply dipping margin of the wedge zone exhibited <sup>EC</sup>:oscillationsa set of linear segments of localized plastic strain. In experiment  $N = 1$  ( $L = 50$  m, Figure 4a), this <sup>EC</sup>:set of <sup>EC</sup>:single sub-vertical <sup>EC</sup>:oscillation in segments of plastic strain had a wavelength of about 6–8 m and was

matched by a narrow, sub-vertical zone of deformation at the right-hand sub-domain boundary.

(c) Prior to the onset of <sup>EC</sup>domain-crossing? strain localization, i.e., rupture, a sub-horizontal wedge of somewhat diffuse plastic strain grew from upper-left corner of the sub-domain towards the right, and in most experiments ( $N \geq 3$ ) the zone <sup>EC</sup>developed oscillations's propagation is accompanied by the appearance of the subvertical localization features on a smaller scale of around 3–4 m. This behavior is evident in Figure 2a and particularly in Figures 1b, 1c. The <sup>EC</sup>band of oscillationsset of subvertical localization features spanned a vertical range of about 15–20 m upper-bounded by the lower, right-propagating main rupture.

<sup>EC</sup>(d) Preliminary investigation of <sup>EC</sup>both [?] <sup>EC</sup>sets of oscillationsthose subvertical localization features suggests they <sup>EC</sup>both represent real physical phenomena, rather than numerical artefacts <sup>EC</sup>; but more study is required before a definitive conclusion can be made. Strong supporting evidence comes from <sup>EC</sup>the consistency with other numerical experiments studying off-fault localization associated with fault tip propagation [Dalguer et al., 2003; Templeton and Rice, 2008], in which <sup>EC</sup>oscillatory plastic deformation wasneedle-like off-fault localization features were also observed. In addition, our subvertical localization features are parallel to sub-parallel with a set of slip lines (Figure 2 and 3), which indicate that they were created as one of the conjugate

sets of shear failure with an orientation close to the Arthur angle.

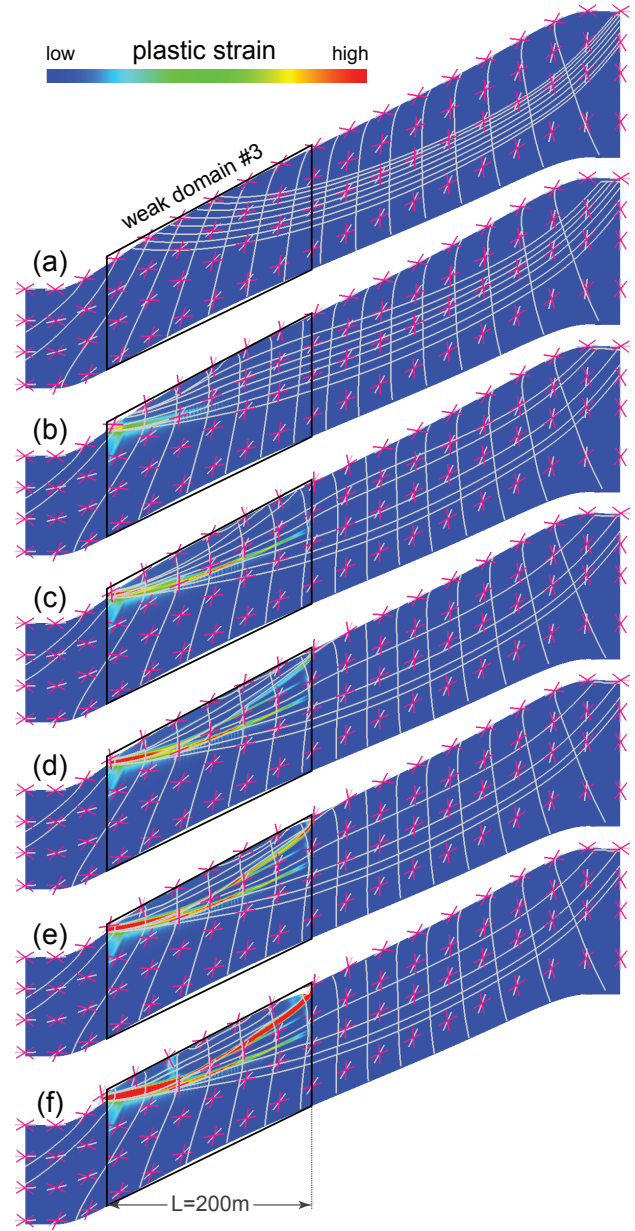


**Figure 2:** Time sequence of slope failure for 200m-wide weak zone showing evolution of <sup>EC</sup>the second invariant of plastic strain <sup>EC</sup>as well as a selected set of conjugate slip lines (white lines) <sup>EC</sup>during plastic deformation.





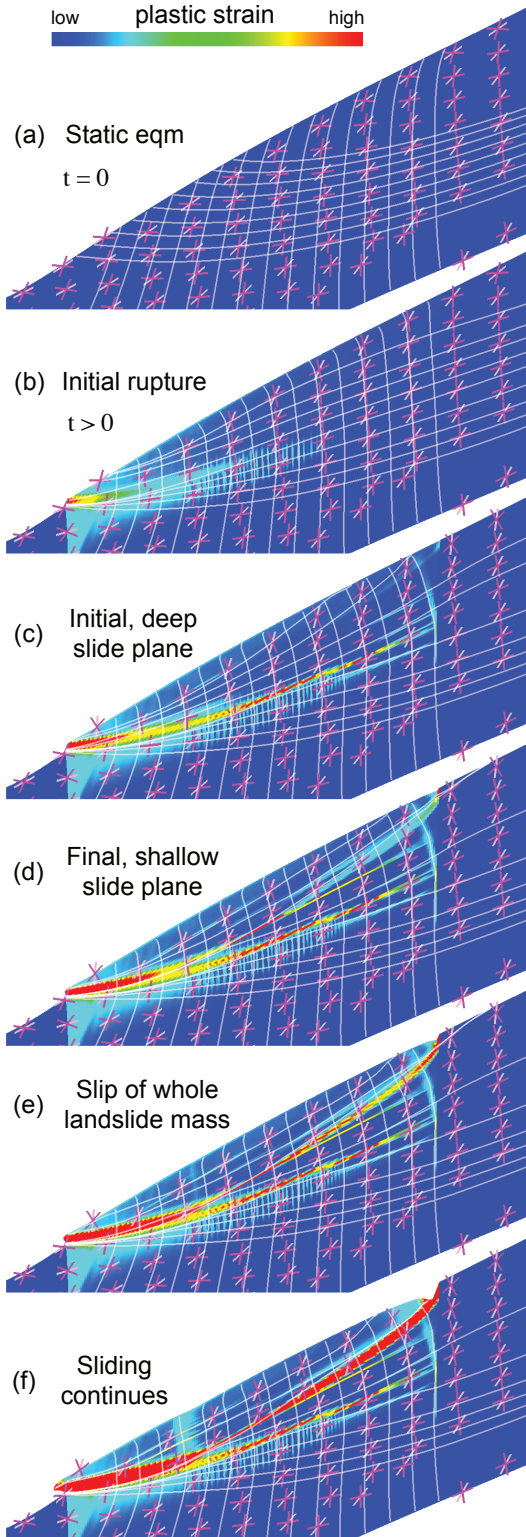


**Figure 3:** Zoom into 200m-wide weak zone in Figure 2 showing history of plastic strain in detail. TBD: notes on stress axis markers, initial deep failure, progressive shallowing of main slide plane, conjugate sub-vertical shear bands, how final main slip plane is not at all given by initial or even later slip lines.

(<sup>EC</sup>:de) A toe zone developed in several of the model landslides between the emergent rupture tip and the point where the linking, downward-growing rupture joined with the initial, upward-growing slip surface. In several of the experiments, particularly  $N = 4$  and  $N = 5$  (Figures 1b, 1c), a sub-vertical shear band developed above this point.

(<sup>EC</sup>:ef) Around this point of inflexion, shear bands were also seen to develop within the landslide body parallel with the upper boundary. In some of the experiments, some of these shear bands linked with ruptures growing from the upper breakaway zone.



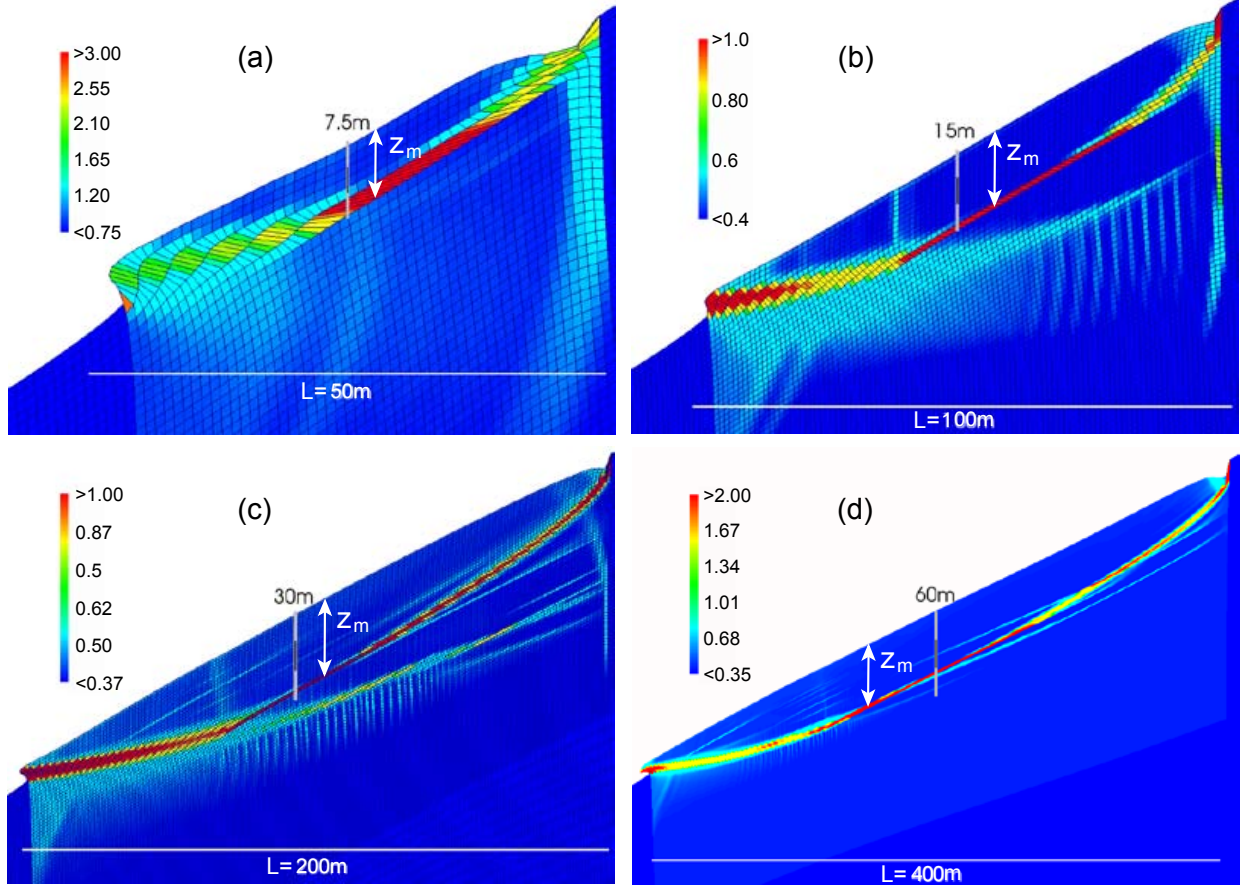


**Figure 4:** Simulated landslide geometries and model plastic strain (colors) (see Table 1): (a)  $L = 50$  m, experiment  $N = 1$ ; (b)  $L = 100$  m, experiment  $N = 4$ ; (c)  $L = 200$  m, experiment  $N = 5$ ; (d)  $L = 400$  m, experiment  $N = 6$ .

### Self-similarity

Our experimental results appear to vindicate the hypothesis of linear scaling between maximum slip depth  $z_m$  and landslide rupture length  $L$  (Table 1, Figure 6;  $z_m$  is measured from the upper boundary vertically down to the base of the main shear zone). Seven of the eight simulations generated a model landslide and their failure geometries were approximately self-similar across the model length scale range  $50 \leq L \leq 400$  m (Figure 4). The span of maximum-depth-length ratios  $\eta = z_m/L$  was found to be around  $\eta \approx 0.11\text{--}0.15 = 11\text{--}15\%$ , which is broadly consistent with the mean depth-length ratios typically seen in field data that range from 5% to 15% and beyond [e.g., Guzzetti *et al.*, 2009; Hovius *et al.*, 1997]. Figure 6 illustrates a linear model fit to the ex-

perimental data with

$$z_m = \eta L \quad \text{where} \quad \eta \approx 0.13 \pm 0.02. \quad (4)$$

An alternative interpretation is that our results are consistent with a weakly non-linear scaling model  $z_m \sim L^\gamma$  where  $\gamma \approx 1.1$ ; regression against such a model generates a slightly better fit than does equation 4. However, there are too few data points and too many experimental complications to permit a more complex interpretation at this point: further experiments will be required across a broader scaling range to explore the issue further.

### 5. Discussion

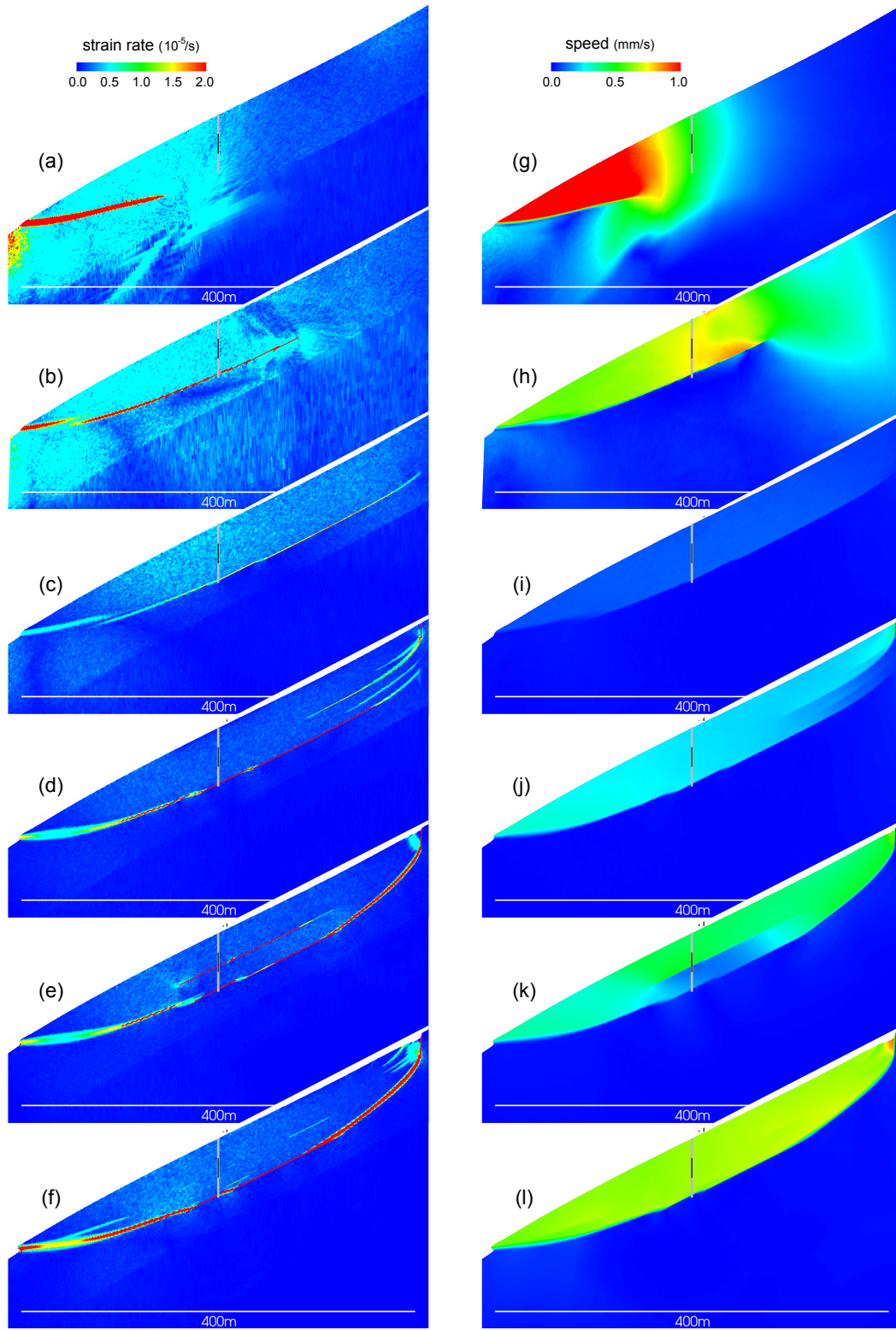


**Figure 5:** TBD. Strain rate during simulated landslide rupture propagation for the largest scale of failure  $L = 400$  m, experiment  $N = 8$  (see Table 1). Time steps shown are: (a)  $t = 1000$  s; (b)  $t = 2000$  s; (c)  $t = 8000$  s; (d)  $t = 16,000$  s. (e)  $t = 20,000$  s. (f)  $t = 24,000$  s. Since strong damping through dynamic relaxation is employed, the amplitude of these strain rates is artificially low, but the patterns are physically correct.

### Representing rupture propagation as strain localization

The use of plastic strain localization as in the current study is justified by the observations that strain localization indicates imminent initiation of fractures in ductile solids [e.g. *Wright*, 2002]. Here, the degree of ductility for which this description holds has a wide range such that shear localization has been perceived as the precursor to full failure (e.g., faulting) even in quasi-brittle solids such as soil and rock [e.g. *Roscoe*, 1970; *Wawersik and Brace*, 1971; *Vardoulakis*, 1979]. Since these experiments show that eventual failure occurs where strain has already been localized, localized strains can be identified with discontinuous internal structures like rupture planes of this study.

We also take the view that the relative motion of the bodies (apparently) separated by localized strain is governed by history-dependent friction between them. In the macroscopic scale, this assumption is materialized in the form of a strain-softening Mohr-Coulomb plasticity. Some authors of landslide research assert that this type of material description is “the most complete and widely accepted approach to model both rock and soil-like materials” [*Crosta et al.*, 2003]. Since the degree of localization is proportional to that of softening, more distributed internal deformation is also described by this constitutive model.

These two ingredients, strain localization in place of discontinuity and history-dependent plasticity, allowed us to follow the standard procedure for modeling the deformation of continua. Although techniques that can directly capture the interactions between particles of granular material are now available (e.g., discrete element method), the continuum-based approach is still widely used, employing well-established numerical techniques like finite element method.

There are known issues with the strain localization in rate-independent plastic solid like the pathological sensitivity to internal mesh alignment [e.g. *Zienkiewicz et al.*, 1995]. However, such erratic behaviors, if present, are often unambiguously recognized. Moreover, SNAC has the redundant discretization scheme that is supposed to remove the effects of the mesh bias.

Strain localization poses other numerical difficulties in a more subtle fashion. For instance, the width of shear band is proportional to the mesh size and some features like the secondary shear zones (Fig. 3) can be resolved only in a sufficiently fine mesh [e.g. *Templeton and Rice*, 2008]. The former is not critical in this study because the rupture widths were significantly smaller than the thickness of <sup>EC</sup> mobilized mass [there might be a better term.] and our mesh was obviously fine enough to resolve the secondary off-rupture plane localization.

One of the fundamental remedies for mesh-dependence of the localization solution within the framework of finite element method is to explicitly add discontinuity in displacements at the element level [e.g.

*Simo et al.*, 1993; *Armero and Garikipati*, 1996; *Borja and Regueiro*, 2001]. This technique is particularly interesting because it allows for quantifying the accuracy of continuum representation of discontinuities with respect to fracture mechanical approaches [*Oliver et al.*, 2012]. The accuracy will be degraded when the above mentioned numerical issues occur and therefore useful to detect

As a separate issue, the Mohr-Coulomb failure criterion is known to provide a less conservative failure indicator than other energy criteria based on fracture mechanics [*Puzrin and Germanovich*, 2005]. However, this fact is irrelevant to our study because we focus on the post-failure behavior of a slope that is unstable by setting.

### Scaling and self-similarity

In some respects, it is not surprising that an elasto-plastic process of hillslope failure should generate landslides whose rupture depth is proportional to rupture length (although the experiments presented here are the first to demonstrate this is the case). The stress field in an elastic body below an arbitrary topographic surface is self-similar [*Iverson and Reid*, 1992; *Martel and Muller*, 2000; *Savage and Swolfs*, 1986], and so the trajectory of most likely failure (such as the surface of least safety factor [*Morgenstern and Price*, 1965]) might be expected to follow the same path regardless of the scale of the domain. However, the process of strain weakening plasticity is non-linear, and the evolution of the stress-strain field close to the propagating rupture tip, specifically the azimuth of maximum weakening, cannot be assumed to behave identically and independently of stress magnitude. What is more, we have chosen a topographic boundary and sub-domain geometry that is not simply rescaled for each experiment, so the elastic stress field is not strictly self-similar for each sub-domain and imposed rupture length (see below).

As was discussed in the introduction, several field studies indicate that landslide cross-sectional geometry should scale in an allometric, or self-affine fashion, with fractional power-law scaling of depth with length. Since our experiments are most consistent with maximum slip depth scaling linearly with rupture length, we deduce that non-linear depth-length scaling originates in material anisotropy such as a depth-dependent variation in shear strength, e.g., in a transition from low-cohesion soils to high-cohesion bedrock, rather than in any anisotropic process of rupture propagation.

**Table 1:** Model parameters and results. The experiment number is  $N$ , the width of the weakened sub-domain is  $L$ , the reduced cohesion imposed in the sub-domain is  $c$  (down from  $c_b = 3$  MPa), the maximum depth of rupture is  $z_m$ , and the ratio of maximum depth to sub-domain length is  $\eta$ . No localized strain weakening deformation and rupture formation was observed in experiment  $N = 2$ .

$N$	Length $L$ (m)	Cohesion $c$ (kPa)	Depth $z_m$ (m)	Ratio $\eta$ (%)
1	50	10	6	12
2	50	20	-	-
3	100	10	13	13
4	100	20	14	14
5	200	20	27	13.5
6	400	20	45	11.25
7	400	25	60	15
8	400	30	61	15.25

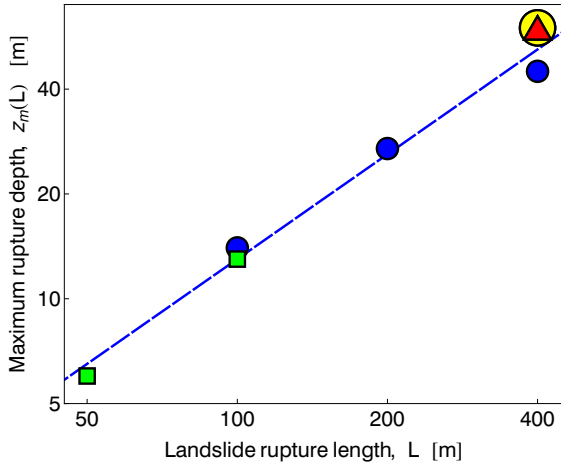


**Figure 6:** Landslide length-depth scaling. A linear model  $z_m = \eta L$  is shown as a blue dashed line with  $\eta = 0.13$ . Green squares:  $c = 10$  kPa (experiments  $N = 1, 3$ ); blue circles:  $c = 20$  kPa (experiments  $N = 4, 5$ ); red triangle:  $c = 25$  kPa (experiment  $N = 7$ ); big yellow circle:  $c = 30$  kPa (experiment  $N = 8$ ).

### Dynamic relaxation, strong damping, and time scales

It is important to bear in mind that even though our simulations solve a momentum equation to track changes in stress, they do not provide solutions for the dynamics of slope failure. This is because of the damping technique of dynamic relaxation employed in our numerical experiments. Dynamic relaxation reduces accelerations such that the static or steady-state stress fields are obtained in a computationally effective but not strictly dynamic manner.

The practical consequence is that stresses acting within the model domain are approximately elastostatic and almost entirely determined by the shape and weight

of the domain (the 3D distribution of body forces) at each time step, i.e., without any significant contribution from the 3D distribution of accelerations. Accelerations during the redistribution of mass therefore have only a weak effect on the patterns of strain rate. Put another way, it is only the change in mass distribution over time that lead to change in stress over time. Model solutions of this kind are termed quasi-static.

Since damping is so strong, the rate of evolution of a zone of plastic strain weakening, i.e., the speed of landslide rupture propagation, is artificially very slow (Figure 5). Rates of landslide motion (Figure 5) are also similarly very slow. However, both rates have physical meaning in that they represent the patterns of deformation and motion if accelerations during failure contribute little to plastic strain localization. To allow SNAC to treat modes of slope failure where dynamics are important to the evolution of plastic strain, alternative methods of damping such as viscous (velocity-dependent) or Rayleigh (modal frequency dependent) damping will need to be implemented [Clough and Penzien, 1993].

### Choice of experimental geometry

The experimental geometry, with its nested sub-domains of cohesion reduction spanning widths of  $L \in \{50\text{m}, 100\text{m}, 200\text{m}, 400\text{m}\}$ , was expressly chosen so as to minimize the effect of surface topography on the stress field, and to mimic the nested, multiscale behavior of failures on single, broad hillslopes seen in multitemporal landslide inventories [Cardinali *et al.*, 2001; Hovius *et al.*, 1997; Galli *et al.*, 2008; Stark and Hovius, 2001; Stark and Guzzetti, 2009]. Such a concern would have been more of an issue in alternate choices of experimental geometry.

For example, Stage 2 weakening could have been applied to the whole model domain, which would have led to failure at the stress concentration on the lower step (Figure 1) and curvilinear rupture propagation towards the upper step (in a fashion seen in many engineering treatments of slope instability). Alternatively, the widest sub-domain could have been used in all the experiments (as in  $N = 6-8$ ), and the scale of the whole domain adjusted along with the size of grid cells (maintaining the same number of grid nodes by adjusting the mesh resolution), leading to failures spanning most of the model ramp every time spanning the requisite range of  $L \in \{50\text{m}, 100\text{m}, 200\text{m}, 400\text{m}\}$ . In both cases, topographic control over the stress field would have been so strong that self-similar failure geometries would inevitably have ensued, but broader conclusions would have been drawn harder to draw.

### Triggering and bottom-up versus top-down failures

The model imposition of a uniform sub-domain of weakening and initial plastic deformation is a simplification that makes broader interpretation of model rupture



behavior difficult. In particular, the pattern of destabilization in natural slopes is much more complex, either by rising pore-fluid pressures following rainwater [Iverson, 2000; Sidle and Ochiai, 2006] or snowmelt infiltration [Guzzetti *et al.*, 2002], or by stress changes induced by earthquake strong-ground motion [Harp and Jibson, 1996; Meunier *et al.*, 2007, 2008; Sidle and Ochiai, 2006]. In fact, Meunier *et al.* [2008] have argued that systematic differences in the geometry of hydrologic versus seismic forcing may lead to systematic differences in the location of landslide initiation and propagation.

In spite of the geometric simplicity of the triggering mechanism, the formation of model landslide ruptures exhibited a two-stage evolution that may provide some insight into the issue of top-down versus bottom-up failures. First, a rupture initiates at the upper left sub-domain corner (toe) and propagates, sub-parallel to the topographic surface, until the right sub-domain boundary is reached; second, a shallower rupture initiates at the upper right corner (breakaway) and grows downwards asymptotically into the first rupture until a connected slip plane is formed and whole landslide motion begins.

It is possible that this behavior is a peculiarity of our model geometry and the simplistic means by which plastic failure is triggered. Nevertheless, it is worth raising the possibility that a two-stage process of slip plane establishment may occur in some real-world landslides.

Several of the secondary deformation phenomena observed in the model may also happen in nature. For example, the development of main-rupture-parallel internal slip surfaces, or the formation sub-vertical shear zones above breaks in slope on the main rupture surface, may both occur in real landslides.

#### Parallel code for modeling slope failure

Our experiments serve as a first test of the parallel code SNAC for the modeling of slope failure and initial landslide motion. The simulations were 2+1D (in the sense that only a narrow cross-sectional mesh was used) but computations were carried out in 3D, they were completed rapidly with 64 processor cores, and scaling up to larger, fully 3D domains will therefore be straightforward. Thus SNAC represents an important new community resource for the study of hillslope instability and incipient deformation on large scales and at high resolution. Given its flexible design, SNAC can readily be extended to handle more realistic mechanisms of instability such as rainwater infiltration and pore fluid pressure rise. Its ability to treat material heterogeneity [Choi *et al.*, 2008] will prove particularly useful in modeling complex hillslopes with a variety of vegetation cover, soil-mantling, weathering depths, bedrock strength, and jointing anisotropy [Sidle and Ochiai, 2006].

## 6. Conclusions

In a series of 2+1D numerical experiments of strain-weakening elastoplastic deformation, we have shown that landslide rupture depth is approximately proportional to rupture length. The ratio of maximum slip depth to rupture length was found to be around 11–15%, and the variability in this value arose from an unanticipated complexity in the rupture process: landslide failure initiated at the toe, but the final slip surface was an amalgam of the upward-propagating rupture and a downward-propagating slip surface whose trajectory varied in response to heterogeneity in the evolving stress-strain field.

Our model treatment was expressly simplified to avoid complexities such as a systematic variations in material properties with depth, spatiotemporal patterns of unloading and instability under realistic triggering mechanisms, and dynamic transfers of stress. It also avoided treating heterogeneity in the stress field arising from rough topographic relief, or heterogeneity in material properties such as randomness in cohesion throughout the domain. These issues are left for future work.

To carry out these experiments, the community code SNAC was adapted for first time to treating a geomorphologic problem. SNAC offers a promising continuum mechanical modeling framework for carrying out these and other experiments on hillslope processes. It also provides the means to do so in 3D in parallelized supercomputing environments.

**Acknowledgments.** Financial support was provided to Stark by the National Science Foundation under grants EAR 08-23953, BCS 10-63231, EAR 11-24114 and EAR 11-50072, and by the Lamont-Doherty Earth Observatory. Financial support was provided to Choi by the National Science Foundation under grant EAR 06-35898. **TKTK: This might need updating.** Computing support was provided by TeraGrid Ranger under pilot project TG-EAR090034.

## Appendix A

### A1. Governing equation

In SNAC, the differential equation for momentum balance is converted into a principle of minimum work rate,

$$\int_{\Omega} \delta v_i \rho \frac{Dv_i}{Dt} dV = \int_{\Omega} \delta v_i \rho g_i dV + \int_{\Omega} \delta \xi_{ij} \sigma_{ij} dV \quad (5)$$

as in the standard finite element (FE) method [Bathe, 1996; Zienkiewicz *et al.*, 2005]. Here  $\xi_{ij}$  are components of the strain rate tensor,  $\delta v_i$  and  $\delta \xi_{ij}$  represent variations of velocity and strain rate, and  $\Omega$  corresponds to the whole domain. The local contribution to nodes corresponding to each term are computed by following the standard finite element procedure for linear tetrahedral elements. The resulting momentum equation is

$$M^n \frac{Dv_i^n}{Dt} = \frac{1}{3} T_i^{[n]} + \frac{1}{4} \rho^{[n]} g_i V^{[n]} \quad (6)$$

where the superscript  $n$  represents values evaluated at the global node  $n$ , the superscript  $[n]$  means the sum of contributions from all the tetrahedra having the global node  $n$  as an apex, and  $T_i$  is the traction that is defined as  $\sigma_{ij}n_j$  and evaluated on a face of one of the contributing tetrahedra.

The nodal mass  $M^n$  is not the true inertial mass, but rather a mass adjusted to satisfy the local stability criterion discussed below (subsection A5 on mass-scaling). The correspondence between an apex and a face for the traction calculation is determined in the same way as equation 9 (see below). Note that in equation 6, the factor of  $\frac{1}{3}$  in the traction term is inherited from equation 9, and the factor of  $\frac{1}{4}$  in the body force term implies that the nodal contribution takes one quarter of a tetrahedron's volume-dependent quantity.

While looping over the entire set of nodes, the mass forces and nodal forces are assembled by summing the contributions from the boundary conditions and all the tetrahedra sharing a node as one of their apices. The structured mesh of SNAC renders this assemblage step straightforward because the nodal neighborhood never changes (a structured mesh has a regular nodal topology in which each cell is simply identified by its  $x$ ,  $y$  and  $z$  indices, whereas an unstructured mesh has an irregular nodal topology whose cells require more complex indexing). The acquired net force at each node is used to update velocities and node coordinates.

### A2. Approximation of partial derivatives

Approximation of partial derivatives with respect to spatial variables follows an integral definition [e.g., Wilkins, 1964],

$$\int_{\Omega} f_{,i} dV = \int_{\partial\Omega} f n_i d\Gamma \quad (7)$$

where  $\Omega$  represents a tetrahedron as an integration domain,  $\partial\Omega$  is the set of boundary surfaces of the tetrahedron,  $f_{,i}$  is the partial derivative of a variable  $f$  with respect to  $i$ -th spatial coordinate, and  $n_i$  is the  $i$ -th component of the unit normal vector of the surface. Assuming the partial derivative is constant within a tetrahedron, it can be evaluated as

$$f_{,i} = \frac{1}{V} \int_{\partial\Omega} f n_i d\Gamma \quad (8)$$

where  $V$  is the volume of the tetrahedron. By further substituting an algebraic expression for the surface integral, reordering terms, and using  $\int_{\partial\Omega} n_i d\Gamma = 0$  (when

$f = 1$  in equation 8),

$$\begin{aligned} f_{,i} &= \frac{1}{V} \sum_{l=1}^4 \bar{f}^l n_i^l A^l = \frac{1}{V} \sum_{l=1}^4 \frac{1}{3} \sum_{m=1, \neq l}^4 f^m n_i^l A^l \\ &= \frac{1}{3V} \sum_{m=1}^4 f^m \sum_{l=1, \neq m}^4 n_i^l A^l \\ &= -\frac{1}{3V} \sum_{m=1}^4 f^m n_i^m A^m \end{aligned} \quad (9)$$

where  $l$  is the local node index varying from 1 to 4,  $A^l$  and  $n^l$  are the area and the unit-normal vector of the triangular surface not having the node  $l$  as one of its apices (Figure 7b). We call such a face a *corresponding* face to node  $l$ . The term  $\bar{f}^l$  is the average of  $f$  over the surface  $l$ .

### A3. Spatial discretization

The 3D model domain is discretized into hexahedral elements, each of which is filled with two sets of five tetrahedra (Figure 7a). In this mesh hierarchy, called the mixed discretization [Marti and Cundall, 1982], hexahedral elements are used largely as an averaging unit for estimating volumetric strain for incompressible viscoelastic or plastic constitutive laws.

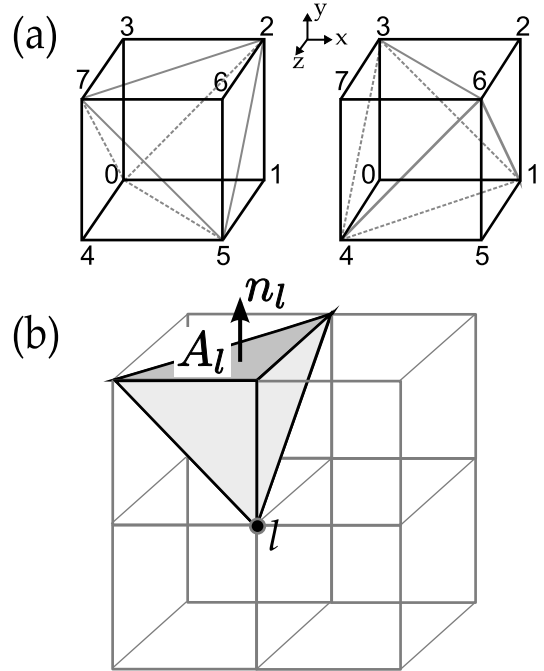


**Figure 7:** Configurations of tetrahedra and notation convention. (a) Two configurations of five tetrahedra in a hexahedral element used in the mixed discretization. Numbers next to apices indicate the local node numbering. (b) Notation.  $A_l$  and  $n_l$  denote the face and the unit normal vector, respectively, associated with a local node  $l$ .



#### A4. Solution scheme

SNAC finds static and quasi-static solutions through a local non-viscous damping scheme called dynamic relaxation [Underwood, 1983], modified slightly from Cundall [1987], in which unbalanced nodal forces (i.e., those driving accelerations) are reduced by a constant fraction

$$F_i^{\text{damped}} = F_i - \alpha \operatorname{sgn}(v_i) |F_i| \quad (10)$$

where  $F_i$  is the  $i$ -th component of the residual force vector (the right hand side of equation 6),  $\alpha$  is a positive coefficient less than 1,  $\operatorname{sgn}(v_i)$  returns the sign of the  $i$ -th component of velocity,  $v_i$ . Once net forces are assembled and damped, velocity at that node is updated using a forward Euler method,

$$v(t + \frac{1}{2}\Delta t) = v(t - \frac{1}{2}\Delta t) + \Delta t \frac{F_i^{\text{damped}}}{M} \quad (11)$$

and

$$x(t + \Delta t) = x(t) + \Delta t v(t + \frac{1}{2}\Delta t) . \quad (12)$$

#### A5. Mass scaling for numerical stability

The conventional Courant-Friedrichs-Lewy (CFL) condition imposes a stringent upper limit for the time step size such that dynamic relaxation takes an excessively large number of time steps to reach a quasi-static solution. To overcome this limit, a mass scaling technique is applied. This technique adjusts each nodal mass such that the stability condition for a user-specified time step can be locally satisfied. The stability condition, however, is not the same as in the CFL condition of  $\Delta t \leq (l_{\min}/v_p)$ , where  $\Delta t$  is the time step,  $l_{\min}$  is the minimum element size, and  $v_p$  is the p-wave velocity. Instead, by treating the elastic continuum as an infinite mass-spring system, we can use a criterion that does not explicitly include length scale and p-wave velocity (see Chapter 9 in Bathe [1996]), and instead write

$$\Delta t \leq \frac{T_s}{\pi} \quad (13)$$

where  $T_s$  is the period of the system,  $2\pi(m/k)^{1/2}$ ,  $m$  is a point mass, and  $k$  is the stiffness of the spring attached to the point mass. Now, reducing the infinite series of masses and springs in one dimension to a single mass-spring system, the stiffness of that single system becomes  $4k$ , leading to an expression for the mass scaling,

$$m \geq k(\Delta t)^2 . \quad (14)$$

For a given size of  $\Delta t$ , the nodal mass is adjusted according to equation 14, automatically satisfying the stability criterion given in equation 13. The value of  $k$  is computed by equating the internal force contribution at a node with  $-ku_i$ ,

$$\frac{1}{3}T_i = -ku_i \quad (15)$$

and by deducing that (with no summation implied)

$$\frac{1}{3}(\lambda + 2\mu)(\epsilon_{ii}\Delta t)n_i A = -k(v_i\Delta t) \quad (16)$$

where only the volumetric contribution from internal forces is taken into account. By substituting the approximation (equation 9) for the partial derivative  $\epsilon_{ii}$  into the above equation and dividing both sides by  $v_i\Delta t$ , we obtain

$$k_i^l = \frac{1}{9V}(\lambda + 2\mu)(n_i^l A^l)^2 \quad (17)$$

where  $l$  is the local index for apices of a tetrahedron, and the surface-related quantities are computed on the corresponding face of the tetrahedron. Finally, the contribution of each tetrahedron to the scaled mass is given as

$$m^l = (\Delta t)^2 \frac{\lambda + 2\mu}{9V} \max[(n_i^l A^l)^2, i = 1, \dots, 3] . \quad (18)$$

As in the standard finite element method, appropriate mappings between local and global indices are required.

#### A6. Constitutive update

SNAC uses a general elastoviscoplastic rheological model to update the Cauchy stress tensor (e.g., Albert *et al.* [2000]). Details of this implementation are given in Choi *et al.* [2008], and the operator-splitting scheme it employs is described by Simo and Hughes [2004]. Here we discuss only the plastic correction for the strain-weakening Mohr-Coulomb model.

If  $\sigma^{\text{tr},n+1}$ , the elastic trial stress for  $t = t_{n+1}$ , is on or within the yield surface, i.e.,  $f(\sigma^{n+1}) \geq 0$ , where  $f$  is the yield function, then it does not need plastic correction. However, if  $\sigma^{n+1}$  is outside the yield surface, then yielding occurs and we project  $\sigma^{n+1}$  onto the yield surface using a return-mapping algorithm [Simo and Hughes, 2004].

For frictional materials, the yield function is generally written as

$$f(\sigma^{n+1}) = q_\phi \sigma_p + c - \tau \quad (19)$$

in which  $\tau$  represents shear stress,  $\sigma_p$  represents normal stress,  $q_\phi$  is a function of the friction angle  $\phi$ , and  $c$  is cohesive strength of the material.

In the case of a Mohr-Coulomb material,  $q_\phi$  is given as  $\tan \phi$ ,

$$\tau = \frac{1}{2}(\sigma_3 - \sigma_1) \cos \phi \quad (20)$$

and

$$\sigma_p = \frac{1}{2}(\sigma_3 + \sigma_1) - \frac{1}{2}(\sigma_3 - \sigma_1) \sin \phi, \quad (21)$$

where  $\sigma_1 \leq \sigma_2 \leq \sigma_3$  are the principal stresses. The actual form of the yield function for *shear failure* used in SNAC is

$$f_s(\sigma_1, \sigma_3) = \sigma_1 - N_\phi \sigma_3 + 2c\sqrt{N_\phi}, \quad (22)$$

where  $N_\phi = \frac{1+\sin\phi}{1-\sin\phi}$  and  $\sqrt{N_\phi} = \frac{\cos\phi}{1-\sin\phi}$ . The *tensile* yield function is defined as

$$f_t(\sigma_3) = \sigma_3 - \sigma_t, \quad (23)$$

where  $\sigma_t$  is the tension cut-off. If the tension cut-off is given as a parameter, then a smaller value between the theoretical limit  $2C/\tan\phi$  and the given value is assigned to  $\sigma_t$ .

To guarantee a unique decision on the mode of yielding (shear versus tensile), we define an additional function,  $h(\sigma_1, \sigma_3)$ , which bisects the obtuse angle made by two yield functions as

$$f_h(\sigma_1, \sigma_3) = \sigma_3 - \sigma_t + \left( \sqrt{N_\phi^2 + 1} + N_\phi \right) \left( \sigma_1 - N_\phi \sigma_t + 2c\sqrt{N_\phi} \right). \quad (24)$$

Once yielding is identified (i.e.,  $f_s < 0$  or  $f_t > 0$ ), the mode of failure (shear or tensile) is decided based on the value of  $h$ : shear failure occurs if  $h < 0$ , tensile failure occurs otherwise.

The flow rule for frictional materials is in general non-associative, i.e., the direction of evolution of stress (in  $\sigma_1, \sigma_3$  space) during plastic flow is not the same as the direction of the vector normal to the yield surface. As in the definitions of yield functions, the plastic flow potential for *shear* failure in the Mohr-Coulomb model can be defined as

$$g_s(\sigma_1, \sigma_3) = \sigma_1 - N_\psi \sigma_3 \quad (25)$$

where  $N_\psi = \frac{1+\sin\psi}{1-\sin\psi}$  and  $\psi$  is the dilation angle. Likewise, the *tensile* flow potential is given as

$$g_t(\sigma_3) = \sigma_3 - \sigma_t \quad (26)$$

In the presence of plasticity, the total strain  $\Delta\epsilon$  is given by

$$\Delta\epsilon = \Delta\epsilon^e + \Delta\epsilon^p \quad (27)$$

where  $\Delta\epsilon^e$  and  $\Delta\epsilon^p$  are the elastic and plastic strain increments respectively. We assume (in SNAC in general) that if plastic yielding occurs there is a negligible contribution from viscous flow to the total strain (in our experiments no viscous deformation was considered at all). The plastic strain increment is  $\Delta\epsilon^p = \beta \frac{\partial g}{\partial \sigma}$ , where  $\beta$  is the magnitude of the plastic flow. The parameter  $\beta$  is determined by the requirement that updated stress state must lie on the yield surface, i.e.,

$$f(\sigma^n + \Delta\sigma^n) = 0 \quad (28)$$

where the superscript  $n$  denotes the  $n$ -th time step, the stress increment,  $\Delta\sigma^n = \mathbf{C} : (\Delta\epsilon^n - \Delta\epsilon^{p,n})$  and  $\mathbf{C}$  is the elastic moduli tensor.

In the principal component representation,  $\sigma_A = a_{AB}^e \epsilon_B$  where  $\sigma_A$  and  $\epsilon_A$  are principal stress and strain, respectively, and  $\mathbf{a}^e$  is a corresponding elastic moduli

matrix of which components are given in terms of the Lamé constants:  $a_{AB}^e = \lambda + 2\mu\delta_{AB}$ . By applying the consistency condition 28 and using  $\sigma^{\text{tr}} = \sigma^n + \mathbf{C} : \Delta\epsilon^n$ , we obtain the following formulae for  $\beta$ :

$$\beta = \frac{\sigma_1^{\text{tr}} - N_\phi \sigma_3^{\text{tr}} + 2c\sqrt{N_\phi}}{a_{1B}^e \frac{\partial g_s}{\partial \sigma_B} - N_\phi a_{3B}^e \frac{\partial g_s}{\partial \sigma_B}} \quad \text{for shear failure} \quad (29)$$

and

$$\beta = \frac{\sigma_3^{\text{tr}} - \sigma_t}{\frac{\partial g_t}{\partial \sigma_B}} \quad \text{for tensile failure.} \quad (30)$$

In the case of strain hardening/softening through cohesion reduction only, the hardening modulus  $H$  is given by  $\frac{\partial c}{\partial \alpha}$ , where  $c$  is cohesion and  $\alpha$  is an internal variable. Then, the flow parameter for shear failure (equation 29) is modified such that the denominator has an extra term,  $2\sqrt{N_\phi}H$ , added.

## References

- Abele, G., Bergsturze in den Alpen: ihre Verbreitung, Morphologie und Folgeerscheinungen, *Wissenschaftliche, Alpenvereinshefte*, 25, 247 pp., 1974.
- Albert, R. A., R. J. Phillips, A. J. Dombard, and C. D. Brown, A test of the validity of yield strength envelope with an elastoviscoplastic finite element model, *Geophysical Journal International*, 140, 399–409, 2000.
- Armero, F., and K. Garikipati, An analysis of strong discontinuities in multiplicative finite strain plasticity and their relation with the numerical simulation of strain localization in solids, *International Journal of Solids and Structures*, 33(20–22), 2863–2885, doi:10.1016/0020-7683(95)00257-X, 1996.
- Barla, G. B., Editorial - numerical and physical modelling of massive rock slope failure, *Rock Mechanics and Rock Engineering*, 41(1), 1–2, doi:10.1007/s00603-008-0164-0, 2008.
- Bathe, K.-J., *Finite Element Procedure*, Prentice-Hall, Upper Saddle River, New Jersey, 1996.
- Borja, R. I., and R. A. Regueiro, Strain localization in frictional materials exhibiting displacement jumps, *Comput. Methods Appl. Mech. Engrg.*, 190, 2555–2580, 2001.
- Brardinoni, F., and M. Church, Representing the landslide magnitude-frequency relation: Capilano River basin, British Columbia, *Earth Surface Processes and Landforms*, 29, 115–124, 2004.
- Brideau, M.-A., D. Stead, and R. Couture, Structural and engineering geology of the East Gate Landslide, Purcell Mountains, British Columbia, Canada, *Engineering Geology*, 84, 183–206, doi:10.1016/j.enggeo.2006.01.004, 2006.
- Brunetti, M. T., F. Guzzetti, and M. Rossi, Probability distributions of landslide volumes, *Nonlinear Processes in Geophysics*, 16, 179–188, www.nonlin-processes-geophys.net/16/179/2009/, 2009.
- Cardinali, M., G. Antonini, P. Reichenbach, and F. Guzzetti, Photo-geological and landslide inventory map for the Upper Tiber River basin, CNR GNDCI publication n. 2154, scale 1:100,000, 2001.
- Choi, E., L. Lavier, and M. Gurnis, Thermomechanics of mid-ocean ridge segmentation, *Physics of the Earth and Planetary Interiors*, 171, 374–386, doi:10.1016/j.pepi.2008.08.010, 2008.
- Clough, R. W., and J. Penzien, *Dynamics of Structures*, 2nd ed., McGraw-Hill, New York, 1993.
- Commend, S., F. Geiser, and L. Tacher, 3D numerical modeling of a landslide in Switzerland, in *Numerical Models in Geomechanics: Proceedings of the Ninth International Symposium on 'Numerical Models in Geomechanics - Numog IX', Ottawa, Canada, 25-27 August 2004*, edited by G. N. Pande and S. Pietruszczak, pp. 595–601, Taylor and Francis, London, 2004.
- Crosta, G. B., and J. J. Clague, Large landslides: Dating, triggering, modelling, and hazard assessment, *Engineering Geology*, 83, 1–3, 2006.

- Crosta, G. B., S. Imposimato, and D. G. Roddeman, Numerical modelling of large landslides stability and runout, *Natural Hazards and Earth System Sciences*, 3, 523–538, 2003.
- Cundall, P. A., Distinct element models of rock and soil structure, in *Analytical and Computational Methods in Engineering Rock Mechanics*, edited by E. T. Brown, chap. 4, pp. 129–163, London: Allen & Unwin, 1987.
- Cundall, P. A., Numerical experiments on localization in frictional materials, *Archive of Applied Mechanics (Ingenieur Archiv)*, 59(2), 148–159, doi:10.1007/BF00538368, 1989.
- Dadson, S. J., et al., Links between erosion, runoff variability and seismicity in the Taiwan orogen, *Nature*, 426, 648–651, 2003.
- Dalguer, L. A., K. Irikura, and J. D. Riera, Simulation of tensile crack generation by three-dimensional dynamic shear rupture propagation during an earthquake, *Journal of Geophysical Research*, 108, 2144, doi:10.1029/2001JB001738, 2003.
- Day, A. S., An introduction to dynamic relaxation (Dynamic relaxation method for structural analysis, using computer to calculate internal forces following development from initially unloaded state), *The Engineer*, 219, 218–221, 1965.
- Dietrich, W. E., and T. Dunne, Sediment budget for a small catchment in mountainous terrain, *Zeitschrift für Geomorphologie*, 29, 191–206, 1978.
- Dietrich, W. E., D. G. Bellugi, L. S. Sklar, J. D. Stock, A. M. Heimsath, and J. J. Roering, Geomorphic transport laws for predicting landscape form and dynamics, in *Prediction in Geomorphology*, *Geophysical Monograph Series*, vol. 135, edited by P. Wilcock and R. Iverson, pp. 103–132, AGU, Washington, D.C., doi:10.1029/135GM09, 2003.
- Evans, S. G., G. S. Mugnozza, A. Strom, and R. L. Herrmanns (Eds.), *Landslides from massive rock slope failure*, NATO Science Series, Springer, 2006.
- Galli, M., F. Ardizzone, M. Cardinali, F. Guzzetti, and P. Reichenbach, Comparison of landslide inventory maps, *Geomorphology*, 94, 268–289, 2008.
- Gerbault, F., A. N. B. Poliakov, and M. Daignières, Prediction of faulting from the theories of elasticity and plasticity: What are the limits?, *Journal of Structural Geology*, 20, 301–320, 1998.
- Guthrie, R., and S. Evans, Analysis of landslide frequencies and characteristics in a natural system, coastal British Columbia, *Earth Surface Processes and Landforms*, 29, 1321–1339, 2004.
- Guzzetti, F., B. D. Malamud, D. L. Turcotte, and P. Reichenbach, Power-law correlations in landslide areas in central Italy, *Earth and Planetary Science Letters*, 195, 169–183, doi:10.1016/S0012-821X(01)00589-1, 2002.
- Guzzetti, F., F. Ardizzone, M. Cardinali, M. Galli, P. Reichenbach, and M. Rossi, Distribution of landslides in the Upper Tiber River basin, central Italy, *Geomorphology*, 86, 105–122, 2008.
- Guzzetti, F., F. Ardizzone, M. Cardinali, M. Rossi, and D. Valigi, Landslide volumes and landslide mobilization rates in Umbria, central Italy, *Earth and Planetary Science Letters*, 279, 222–229, doi:10.1016/j.epsl.2009.01.005, 2009.
- Harp, E. L., and R. W. Jibson, Landslides triggered by the 1994 Northridge, California, earthquake, *Bulletin of the Seismological Society of America*, 86, S319–S332, 1996.
- Hodgkins, W. R., On the relation between dynamic relaxation and semi-iterative matrix methods, *Numerische Mathematik*, 9, 446–451, doi:10.1007/BF02162158, 1967.
- Hovius, N., and C. P. Stark, Landslide-driven erosion and topographic evolution of active mountain belts, in *Landslides from Massive Rock Slope Failure*, *NATO Science Series*, vol. 49, edited by S. G. Evans, G. S. Mugnozza, A. Strom, and R. L. Herrmanns, chap. 8, pp. 573–590, Springer, Netherlands, 2006.
- Hovius, N., C. P. Stark, and P. A. Allen, Sediment flux from a mountain belt derived by landslide mapping, *Geology*, 25(3), 231–234, 1997.
- Imaizumi, F., and R. C. Sidle, Linkage of sediment supply and transport processes in Miyagawa Dam catchment, Japan, *Journal of Geophysical Research*, 112, F03,012, doi:10.1029/2006JF000495, 2007.
- Imaizumi, F., R. Sidle, and R. Kamei, Effects of forest harvesting on the occurrence of landslides and debris flows in steep terrain of central Japan, *Earth Surface Processes and Landforms*, 33, 827–840, doi:10.1002/esp.1574, 2008.
- Innes, J., Lichenometric dating of debris-flow deposits in the Scottish Highlands, *Earth Surface Processes and Landforms*, 8, 579–588, 1983.
- Iverson, R. M., Landslide triggering by rain infiltration, *Water Resources Research*, 36(7), 1897–1910, 2000.
- Iverson, R. M., and M. E. Reid, Gravity-driven groundwater flow and slope failure potential. I: Elastic effective stress model, *Water Resources Research*, 28, 925–938, 1992.
- Kelsey, H. M., A sediment budget and an analysis of geomorphic processes in the van duzen river basin, north coastal California: 1941–1975, summary, *Geol. Soc. Amer. Bull., Part 1*, 91, 190–195, 1980.
- Korup, O., Distribution of landslides in southwest New Zealand, *Landslides*, 2, 43–51, 2005.
- Korup, O., Effects of large deep-seated landslides on hillslope morphology, western Southern Alps, New Zealand, *Journal of Geophysical Research*, 11, F01,018, doi:10.1029/2004JF000242, 2006.
- Larsen, I. J., and D. R. Montgomery, Global landslide volume-area scaling relationships and implications for landslide erosion, *AGU Fall Meeting Abstracts*, pp. F878+, 2008.
- Lavé, J., and D. Burbank, Denudation processes and rates in the Transverse Ranges, southern California: Erosional response of a transitional landscape to external and anthropogenic forcing, *Journal of Geophysical Research*, 109, F01,006, doi:10.1029/2003JF000023, 2004.
- Lavier, L. L., W. R. Buck, and A. N. B. Poliakov, Factors controlling normal fault offset in an ideal brittle layer, *Journal of Geophysical Research*, 105(B10), 23,431–23,442, 2000.
- Li, X.-Z., J.-M. Kong, and Q. Xu, Deformation and development tendency of Shiliushubao landslide by numerical modeling, *Wuhan University Journal of Natural Sciences*, 11(4), 840–846, 2006.
- Malamud, B. D., D. L. Turcotte, F. Guzzetti, and P. Reichenbach, Landslides, earthquakes, and erosion, *Earth and Planetary Science Letters*, 229, 45–59, doi:10.1016/j.epsl.2004.10.018, 2004a.
- Malamud, B. D., D. L. Turcotte, F. Guzzetti, and P. Reichenbach, Landslide inventories and their statistical properties, *Earth Surface Processes and Landforms*, 29(6), 687–711, doi:10.1002/esp.1064, 2004b.
- Martel, S. J., Modeling elastic stresses in long ridges with the displacement discontinuity method, *Pure and Applied Geophysics*, 157, 1039–1057, 2000.
- Martel, S. J., and J. R. Muller, A two-dimensional boundary element method for calculating elastic gravitational stresses in slopes, *Pure and Applied Geophysics*, 157, 989–1007, 2000.
- Marti, J., and P. A. Cundall, Mixed discretization procedure for accurate modelling of plastic collapse, *Int. J. Numer. Anal. Methods Geomech.*, 6, 129–139, 1982.
- Martin, Y., K. Rood, J. Schwab, and M. Church, Sediment transfer by shallow landsliding in the Queen Charlotte Islands, British Columbia, *Canadian Journal of Earth Sciences*, 39(2), 189–205, 2002.
- Meunier, P., N. Hovius, and J. A. Haines, Regional patterns of earthquake-triggered landslides and their relation to ground motion, *Geophysical Research Letters*, 34, L20,408, doi:10.1029/2007GL031337, 2007.
- Meunier, P., N. Hovius, and J. A. Haines, Topographic site effects and the localization of earthquake-induced landslides, *Earth and Planetary Science Letters*, 275, 221–232, doi:10.1016/j.epsl.2008.07.020, 2008.
- Morgenstern, N. R., and V. E. Price, The analysis of the stability of general slip surfaces, *Géotechnique*, 15(1), 79–93, 1965.
- Muller, J. R., and S. J. Martel, Numerical models of translational landslide rupture surface growth, *Pure and Applied Geophysics*, 157, 1009–1038, 2000.
- Ohmori, H., and M. Hirano, Magnitude, frequency and geomorphological significance of rocky mud flows, landcreep and the collapse of steep slopes, *Zeitschrift für Geomorphologie*, 15, 1–16, 1988.
- Oliver, J., a.E. Huespe, and I. Dias, Strain localization, strong discontinuities and material fracture: Matches and mismatches, *Computer Methods in Applied Mechanics and Engineering*, 241–244, 323–336, doi:10.1016/j.cma.2012.06.004, 2012.
- Otter, J. R. H., Computations for prestressed concrete reactor pressure vessels using dynamic relaxation, *Nuclear Structural Engineering*, 1(1), 61–75, doi:10.1016/0369-5816(65)90097-9, 1965.

- Otter, J. R. H., A. C. Cassell, and R. E. Hobbs, Dynamic relaxation, *Proceedings of the Institution of Civil Engineers*, 35, 633–656, 1966.
- Pasculli, A., and N. Sciarra, A 3D landslide analyses with constant mechanical parameters compared with the results of a probabilistic approach assuming selected heterogeneities at different spatial scales, *Giornale di Geologia Applicata*, 3, 269–280, doi:10.1474/GGA.2006-03.3-35.0128, 2006.
- Poisel, R., H. Angerer, M. Pöllinger, T. Kalcher, and H. Kittl, Mechanics and velocity of the Lärchberg-Galgenwald landslide (Austria), *Engineering Geology*, doi:10.1016/j.enggeo.2009.01.002, 2009.
- Poliakov, A. N. B., H. J. Herrmann, Y. Y. Podladchikov, and S. Roux, Fractal plastic shear bands, *Fractals*, 2(4), 567–581, doi:10.1142/S0218348X9400079X, 1994.
- Puzrin, A., and L. Germanovich, The growth of shear bands in the catastrophic failure of soils, *Proceedings of the Royal Society A: Mathematical, Physical and Engineering Sciences*, 461(2056), 1199–1228, doi:10.1098/rspa.2004.1378, 2005.
- Quenette, S. M., B. F. Appelbe, M. Gurnis, L. J. Hodkinson, L. Moresi, and P. D. Sunter, An investigation into design for performance and code maintainability in high performance computing, *ANZIAM J.*, 46(E), C101–C116, 2005.
- Rice, J. R., The localization of plastic deformation, in *Theoretical and Applied Mechanics (Proceedings of the 14th International Congress on Theoretical and Applied Mechanics, Delft, The Netherlands, 30 August–4 September 1976)*, pp. 207–220, North-Holland, New York, 1976.
- Rice, R. M., and G. T. Fogg, Effects of high intensity storms on soil slippage on mountainous watersheds in Southern California, *Water Resources Research*, 7(6), 1485–1496, 1971.
- Roscoe, K., The influence of strains in soil mechanics, *Geotechnique*, 20(2), 129–170, 1970.
- Rudnicki, J. W., A class of elastic plastic constitutive laws for brittle rock, *Journal of Rheology*, 28(6), 759–778, 1984.
- Rudnicki, J. W., and J. R. Rice, Conditions for the localization of deformation in pressure-sensitive dilatant materials, *J. Mech. Phys. Solids*, 23, 371–394, 1975.
- Savage, W. Z., and H. S. Swolfs, Tectonic and gravitational stress in long symmetric ridges and valleys, *Journal of Geophysical Research*, 91, 3677–3685, 1986.
- Sidle, R. C., and H. Ochiai, *Landslides: Processes, Prediction, and Land Use*, *Water Resources Monograph*, vol. 18, AGU, Washington, DC, doi:10.1029/18WM01, 2006.
- Simo, J., and T. J. R. Hughes, *Computational Inelasticity*, Springer, 2004.
- Simo, J. C., J. Oliver, and F. Armero, An analysis of strong discontinuities induced by strain-softening in rate-independent inelastic solids, *Computational Mechanics*, 12(5), 277–296, doi:10.1007/BF00372173, 1993.
- Simonett, D. S., Landslide distribution and earthquakes in the Bewani and Torricelli Mountains, New Guinea, in *Landform studies from Australia and New Guinea*, edited by J. A. Jennings and J. A. Mabbutt, chap. 4, pp. 64–84, ANU Press, Canberra, 1967.
- Stark, C. P., and F. Guzzetti, Landslide rupture and the probability distribution of mobilized debris volumes, *Journal of Geophysical Research*, 114, F00A02, doi:10.1029/2008JF001008, 2009.
- Stark, C. P., and N. Hovius, The characterization of landslide size distributions, *Geophysical Research Letters*, 28(6), 1091–1094, doi:10.1029/2000GL008527, 2001.
- Stead, D., E. Eberhardt, and J. S. Coggan, Developments in the characterization of complex rock slope deformation and failure using numerical modelling techniques, *Engineering Geology*, 83, 217–235, 2006.
- Sugai, T., and H. Ohmori, Morphometrical characteristics of landslide masses and their geomorphological implications, *Transactions, Japanese Geomorphological Union*, 15(1), 1–16, 1994.
- Templeton, E. L., and J. R. Rice, Off-fault plasticity and earthquake rupture dynamics: 1. Dry materials or neglect of fluid pressure changes, *Journal of Geophysical Research*, 113, B09,306, doi:10.1029/2007JB005529, 2008.
- Underwood, P., Dynamic relaxation, in *Computational Methods for Transient Analysis*, edited by T. Belytschko and T. J. Hughes, Computational methods in mechanics; v. 1. Mechanics and mathematical methods., chap. 5, pp. 245–265, North-Holland, New York, 1983.
- Vardoulakis, I., Bifurcation analysis of the triaxial test on sand samples, *Acta Mechanica*, 32(1-3), 35–54, doi:10.1007/BF01176132, 1979.
- Vermeer, P., and R. de Borst, Non-associated plasticity for soils, concrete and rock, *Heron*, 29(3), 1–62, 1984.
- Wawersik, W. R., and W. F. Brace, Post-failure behavior of a granite and diabase, *Rock mechanics*, 3(2), 61–85, doi:10.1007/BF01239627, 1971.
- Whitehouse, I. E., Distribution of large rock avalanche deposits in the central Southern Alps, New Zealand, *N.Z. Journal of Geology and Geophysics*, 26, 271–279, 1983.
- Wilkins, M. L., Calculation of elastic-plastic flow, *Methods of Computational Physics*, 3, 211–263, 1964.
- Wright, T., *The Physics and Mathematics of Adiabatic Shear Bands*, 260 pp., Cambridge University Press, 2002.
- Wyllie, D. C., and C. W. Mah, *Rock Slope Engineering: Civil and Mining*, UK Spon Press, London, 2004.
- Zienkiewicz, O. C., M. Huang, and M. Pastor, Localization problems in plasticity using finite elements with adaptive remeshing, *Int. J. Numer. Anal. Methods Geomech.*, 19, 127–148, 1995.
- Zienkiewicz, O. C., R. L. Taylor, and J. Zhu, *The Finite Element Method: Its Basis and Fundamentals*, 6 ed., 752 pp., Butterworth-Heinemann, 2005.

---

C. P. Stark, Lamont-Doherty Earth Observatory of Columbia University, 61 Route 9W, Palisades, NY 10964, USA. (cstark@ldeo.columbia.edu)

E. Choi, Lamont-Doherty Earth Observatory of Columbia University, 61 Route 9W, Palisades, NY 10964, USA. (cstark@ldeo.columbia.edu)